Tectonic Regime as a Control Factor for Crustal Fault Zone (CFZ) Geothermal Reservoir in an Amagmatic System

Duwiquet Hugo[1], Fabien Magri[2], Simon Lopez[3], Théophile Guillon[4], Laurent Arbaret[5], Mathieu Bellanger[6], and Laurent Guillou-Frottier[4]

[1]BRGM/ISTO/ TLS-Geothermics
[2]FU Berlin
[3]Bureau des Recherches Geologiques et Minieres
[4]BRGM
[5]University of Orléans, CNRS, BRGM UMR 7327
[6]tls-geothermics

November 21, 2022

Abstract

The Crustal Fault Zones provides an interesting geological target for high temperature geothermal energy source in naturally deep-fractured basement areas. Field and laboratory studies have already shown the ability of these systems to let fluid flow down to Brittle-Ductile-Transition. However, several key questions about exploration still exist, in particular the fundamental effect of tectonic regimes on fluid flow in fractured basement domains. Based on poroelasticity assumption, we considered an idealized 3D geometry and realistic physical properties. We examined a model with no tectonic regime (benchmark experiment) and a model with different tectonic regimes applied. Compared to the benchmark experiment, the results suggest that different tectonic regimes cause pressure changes in the fault/basement system. The tectonic-induced pressure changes affect fluid patterns, onset of convection as well as the spatial extent of thermal plumes and the intensity of the temperature anomalies.

1

Tectonic Regime as a Control Factor for Crustal Fault Zone (CFZ) Geothermal Reservoir in an Amagmatic System

H. Duwiquet[1,2,3], F. Magri[4,5], S. Lopez[1], T. Guillon[1], L. Arbaret[2], M. Bellanger[3], and L. Guillou-Frottier[1,2]

[1]BRGM, Georesources Division, Av. C. Guillemin, BP 36009, F-45060 Orléans Cedex 2, France.

[2]ISTO, UMR 7327, University of Orléans, CNRS, BRGM, 1A Rue de la Férollerie, 45071, Orléans, France.

[3]TLS-Géothermics, 91 Chemin de Gabardie, 31200 Toulouse, France.

[4]Department of Environmental Informatics (ENVINF), Helmholtz Centre for Environmental Research (UFZ), Leipzig, Germany.

[5]Freie Universität Berlin, Department of Hydrogeology, Berlin, Germany.

Corresponding author: Hugo Duwiquet (hugo.duwiquet@gmail.com)

Key Points:

- As a potential geothermal reservoir, crustal fault zones remain largely unexplored and therefore unexploited.

- Different tectonic regimes influence fluid flow.

- The poroelasticity driven force explains why strike-slip CFZs could be considered as interesting targets for geothermal power system.

23 **Abstract**

24 The Crustal Fault Zones provides an interesting geological target for high temperature
25 geothermal energy source in naturally deep-fractured basement areas. Field and laboratory
26 studies have already shown the ability of these systems to let fluid flow down to Brittle-Ductile-
27 Transition. However, several key questions about exploration still exist, in particular the
28 fundamental effect of tectonic regimes on fluid flow in fractured basement domains. Based on
29 poroelasticity assumption, we considered an idealized 3D geometry and realistic physical
30 properties. We examined a model with no tectonic regime (benchmark experiment) and a model
31 with different tectonic regimes applied. Compared to the benchmark experiment, the results
32 suggest that different tectonic regimes cause pressure changes in the fault/basement system. The
33 tectonic-induced pressure changes affect fluid patterns, onset of convection as well as the spatial
34 extent of thermal plumes and the intensity of the temperature anomalies.

35 **1 Introduction**

36 Usually, the formation of a geothermal resource requires the presence of fluid, a drain and
37 a heat source. Permeable faults are natural drains for fluids circulation and have a rising
38 scientific and economic interest for mineral (e.g. lithium) and geothermal resources
39 (Saevarsdottir et al., 2014; Liang et al., 2018, Guillou-Frottier et al., 2020). Crustal Fault Zones
40 (CFZ) are geological structures that localize deformation (Ben-Zion and Rovelli, 2014) and
41 modify the petrophysical properties of the crust above Brittle-Ductile-Transition (BDT). CFZ
42 are defined by faults network and interconnected fractures which extension vary from of a few
43 meters to several kilometers. Field and laboratory observations show a succession of damage
44 zones and fault cores corresponding to the multiple fault core conceptual model of Faulkner et al.
45 (2003). Within the interconnected fracture networks of the Pontgibaud Crustal Fault Zone, the
46 presence of pores at different scales (from 2.5 µm to 2 mm) facilitates fluid flow (Duwiquet et
47 al., 2021). CFZ are widely present around the globe. They are found in Chile - Atacame Fault
48 System - (Mitchell and Faulkner, 2009), Germany - Badenweiler-Lenzkirch Sutur – (Brockamp
49 et al., 2015), or Finland - Pasmajärvi Fault Zone - (Ojala et al., 2019). These geological
50 structures can be located in different geological settings (magmatic or amagmatic) and different
51 tectonic stress regimes. This paper investigates the role of the tectonic regime on geothermal
52 reservoirs within and around CFZ, in amagmatic systems.
53
54 Although CFZ provide potential renewable and economic geothermal resources, they remain
55 largely unexplored and undeveloped. Thus, full understanding of the processes that impact fluid
56 flow in CFZ is a prerequisite for successful exploration. Recent work has shown that pressure
57 and temperature conditions can induce fluid flow near the BDT (Violay et al., 2017; Watanabe et
58 al., 2017; 2021). Fluid-filled fractures have been observed down to mid-crustal depths, as shown
59 by the deep boreholes of the Kola Peninsula (Kozlovsky, 1984), and the German KTB
60 continental deep drill hole (Grawinkel and Stöckhert, 1997; Ito and Zoback 2000). Additionally,
61 Famin et al. (2004) suggested that massive infiltration of surface-derived fluids occurred in a
62 detachment shear zone of Tinos Island (Greece), down to a depth of 10-15 km. Similarly,
63 Siebenaller et al. (2013) demonstrated that meteoric fluid infiltration occurs down to the BDT
64 (around a depth of 8 km) in the Naxos detachment fault (Greece).
65
66 Convection around geothermal wells is mandatory to reach production power that leverage the
67 high drilling cost of deep borehole. When the permeability is too low, the strategies developed

68 by the Enhanced Geothermal System (EGS) technique increase the permeability by different
69 injection phases, among which hydraulic stimulations aim at causing hydro-shearing and/or
70 hydro-fracturing. These methods have allowed the development of many geothermal power
71 plants, such as Soultz-sous-Forêts, Upper Rhine Graben, France (Genter et al., 2010). However,
72 the seismicity induced by these injection phases have jeopardized several geothermal projects
73 (Deichmann and Giardini, 2009, Evans et al., 2005). Between 2020 and 2021 in Alsace (France)
74 a series of induced earthquakes of magnitude M=3, M=3.6, M=3.9 caused the definitive
75 shutdown of the geothermal project and raised doubts in the population. Since 2020, the United
76 Downs Deep Geothermal Project (UDDGP) is attempting to target a naturally fractured reservoir
77 in the heat-producing Cornish granite (Ledingham et al., 2019; Paulillo et al., 2020). Drilling
78 through the sub-vertical, strike-slip Porthtowan fault zone has induced an earthquake of
79 magnitude M = 1.5 (www.inducedearthquakes.org), too small to be felt by local population.
80 These naturally fractured zones can then be areas where the risk of induced seismicity is limited.
81
82 The complex nature of the interactions between Thermal (T), Hydraulical (H), Mechanical (M)
83 and Chemical (C) couplings affect the behavior of the geothermal reservoir under natural
84 conditions. Numerical modeling has been used since 1945 to understand the controlling factors
85 of fluid circulations (Horton and Rogers, 1945; Katto & Masuoka, 1967; Horne, 1979; Forster &
86 Smith, 1989; López & Smith, 1995; O'Sullivan et al., 2001; Magri et al., 2016; Guillou-Frottier
87 et al., 2020). Tectonic deformation has been considered as driving forces that influence fluid
88 flow in different geological contexts (Ord and Oliver, 1997b; Cox, 1999; Rowland and Sibson,
89 2004). Bethke (1985) shows that compressive environments can lead to increased fluid pressure
90 and favor upward movement. Sibson (1987) links overpressure and upward movement to fault
91 valve activity. In extensional environments, the generated under-pressure appears to cause
92 downward fluid migration (McLellan et al., 2004). Nevertheless, none of them have looked at the
93 effect of tectonic regime on fluid flow, and the consequences on the temperature anomalies in
94 CFZ. Cui et al. (2012) used simplified 2D models with a fault zone to show that with degrees of
95 shortening exceeding 1% the fluid flows whose driving force was buoyancy forces is then
96 different. In 3D models, Eldursi et al. (2020) suggest that during tectonically active periods, the
97 decrease in pore pressure can reorient fluid flow in fractured zones.
98
99 Fluid flow velocities, and thus efficiency of heat transport by convection through the crust, are
100 directly controlled by the permeability of the rocks. Permeability is a dynamic and variable
101 parameter that can change during different geological processes (Gleeson and Ingebritsen, 2016).
102 The relationship between permeability and porosity is widely debated. Although adapted to
103 porous media, the Kozeny-Carman relationship does not seem appropriate for fractured media
104 (Lamur et al., 2017; Parisio et al., 2019).
105
106 In CFZs, fluid circulation driven by buoyancy forces occurs through upward and downward
107 movement localizing positive temperature anomalies at shallow depths (Duwiquet et al., 2019;
108 Guillou-Frottier et al., 2020). These 2D and 3D TH numerical modeling studies have shown that
109 vertical or subvertical deep deformation zones could concentrate the most important temperature
110 anomalies at the lowest depths. However, these results do not consider poroelastic effects on
111 fluid flow. Poroelastic models describe the interaction between fluids and deformation in the
112 porous medium. The fluids in a reservoir are affected by stresses whether on their pressure
113 (undrained conditions in low-permeable media with, e.g., increase in pressure under compressive
114 stress state), or on their circulation (drained conditions in permeable media with, e.g., convection

115 from more to less compressed regions). Our previous study, which includes poroelasticity,
116 suggested that vertical deformation zones oriented at 30° and 70° to a maximum horizontal stress
117 could correspond to potential targets for high temperature geothermal energy (Duwiquet et al.,
118 2021). Thus, the stress orientation has an effect on the fluid flow. In anisotropic boundary
119 conditions, these effects are expected to be strongly accentuated. Indeed, they introduce shearing
120 conditions favorable to dilation. These aspects could be treated in mechanical terms, which
121 would allow the calculation of slip tendency, defined by the ratio of shear stress and effective
122 normal stress (Morris et al., 1996).

124 Here, we investigate, the role of tectonic regimes on the formation of an amagmatic geothermal
125 reservoir (i.e. the only heat is the natural geothermal flux) within a CFZ and without any other
126 heat source than the natural geothermal flux (amagmatic system). We propose a faulted 3D THM
127 numerical model with a simplified geometry. The physical properties are realistic and the
128 hydraulic permeability is adapted to the fractured environment. In order to understand the role of
129 tectonic regimes, we first considered a benchmark experiment that neglects tectonic stress. This
130 result is compared to several numerical experiments where tectonic stresses are implemented.

132 The effect of the poroelasticity-driven force on fluid flow will differ from one tectonic regime to
133 another and impact the formation of a HT geothermal reservoir in fractured environment. The
134 observed differences can be mainly explained by different lateral fluid pressure variation. This
135 paper highlights the importance of mechanical effects in geothermal processes. The tectonic
136 induced pressure changes affect fluid patterns, onset of convection, the spatial extent of thermal
137 plumes and the intensity of the temperature anomalies.

2 Materials and Methods

139 Comsol Multiphysics^{TM} software is based on the Finite Element Method (FEM) and can,
140 among other various physical processes, model fluid flow, heat transfer and elastic deformation
141 of materials in a 3D geometry. Comsol Multiphysics^{TM} is a well-known tool offering a complete
142 access to the solution of partial differential equations. Benchmark tests have already been
143 performed with previous numerical codes (OpenGeoSys, Comsol Multiphysics^{TM} v3.5a, see
144 Guillou-Frottier et al., 2020 and Appendix 1).
145 We consider an idealized and synthetic model that represents a typical vertical fault zone of 400
146 m thickness, in the middle of a 5.5 km side cubic volume of homogeneous basement rock. The
147 fault zone, which corresponds to a multiple fault core, is treated like continuous porous medium.
148 At very high fracture density, this assumption seems to be convenient (Zareidarmiyan et al.,
149 2021). The mesh is defined by 15,785 tetrahedra, with mesh sizes of 500 m for low permeability
150 zones and mesh sizes of 170 m for high permeability zones. Preliminary convergence tests have
151 shown that a finer mesh size gives the same results. The transient simulations are run up to 990
152 kyrs. The vertical faces of the basement are thermally insulated and fluid circulation is blocked.
153 On the upper horizontal face, a temperature of 20°C and a pressure of 105 Pa are imposed (Fig
154 1).
155 The initial thermal regime corresponds to a geothermal gradient of 30°C/km. At the base of the
156 model a heat flux of 100 mW.m^{-2} is imposed. This heat flux can represent the sum of the mantle
157 heat flow and the heat emitted by the decay of radioactive elements in the crust. The fluid is
158 assumed to be pure water, and the fluid density depends on the pressure and temperature
159 conditions (as detailed in Duwiquet et al., 2021). The details of the equations between Darcy's

160 law, Fourier's law and Hooke's law can also be found in Duwiquet et al. (2021). All thermal,
161 hydraulic and mechanical parameters are detailed in Table 1:
162
163 **Table 1 : Set of physical parameters used in numerical modelling. *Fault zone**
164 **permeability is variables and adapted to fractured media (see Eq 3).**
165

Category	Symbols	Fault zone	Basement	Unit
Porosity	Φ	0.1	0.05	-
Permeability	k	Variable*	10^{-16}	m^2
Thermal conductivity	λ_s	3	2	W/(m.K)
Heat capacity	Cp_s	800	800	J/(kg.K)
Bulk density	ρ_s	2700	2700	kg/m^3
Young's modulus	E	5	60	GPa
Poisson's ratio	v	0.30	0.25	-
Biot-Willis coefficient	α_B	0.8	0.8	-

166
167 The Young's moduli imposed in the numerical models are suitable for fault zone and basement
168 (Cappa and Rutqvist, 2011). In the basement, the Poisson's ratio is 0.25, a value generally
169 accepted in the literature. However, in the fault zone we impose a value of 0.30. This value can
170 be explained by two aspects, the first one is that the samples on which the Poisson coefficients
171 are measured are much smaller than the block considered. This change of scale tends to increase
172 the value of the Poisson coefficient (Heap et al., 2020). In addition, weathering and fracturing
173 processes present in fault zones tend to increase the value of the Poisson's ratio (Heap et al.,
174 2020). The physical properties of the fluids are identical to the study by Duwiquet et al. (2021).
175
176 In order to investigate the influence of tectonic regimes on fluid flow, we will compare a model
177 with no tectonic stresses applied (which we will call the "benchmark experiment") with models
178 where different tectonic regimes are considered. For these models, we have free boundary
179 condition at the top, and clamping at the bottom (displacement blocked in all three directions).
180 For the four vertical sides of the model, we use mechanical boundary conditions corresponding
181 to the evolution of the stress with depth for different tectonic regimes. For this, we refer to an
182 Andersonian assumption -where the principal stresses are expressed with vertical Sv, maximum
183 horizontal SHmax and minimum horizontal Shmin components- which is regularly used in
184 geomechanical studies of reservoirs (Anderson, 1905; Zoback et al., 2003):
185
186   - Compressional (reverse/thrust faulting), $S_{Hmax} \geq S_{hmin} \geq S_V$
187
188   - Extensional (normal faulting) with, $S_V \geq S_{Hmax} \geq S_{hmin}$
189
190   - Strike-slip, with, $S_{Hmax} \geq S_V \geq S_{hmin}$

In order to understand the possible effects of stress intensity, stress-depth profiles were collected on two natural systems, one in the French Massif Central, and one near the San Andreas Fault. Two cases are considered, a low stress intensity zone (e.g. French Massif Central) and a high stress intensity zone (e.g. San Andreas Fault). It should be noted that we assume that regional stresses prevail over local stress variations, which is consistent with our homogeneity assumption. The stress profiles as a function of depth correspond to the following equations (Cornet & Burlet, 1992; Zoback, 1992):

High stress intensity:

$$\sigma_3 = 1 \times 10^6 + (15000 \times (-z))$$

$$\sigma_2 = 4 \times 10^6 + (20000 \times (-z)) \hspace{3cm} \text{Eq 1}$$

$$\sigma_1 = 7.5 \times 10^6 + (28667 \times (-z))$$

Low stress intensity:

$$\sigma_3 = 0.1 \times 10^6 + (13975 \times (-z))$$

$$\sigma_2 = 0.1 \times 10^6 + (26225 \times (-z)) \hspace{3cm} \text{Eq 2}$$

$$\sigma_1 = 0.1 \times 10^6 + (28725 \times (-z))$$

where σ_1, σ_2, σ_3, are the maximum, intermediate and minimum principal stresses, respectively. z is the vertical upwards axis, and an increase in depth ($z < 0$) brings a more compressive stress (positive compression convention). We assume the constant evolution of the stress with depth. The red color code corresponds to the high stress intensity and green color code corresponds to low stress intensity. Notice that in their natural state, a strike-slip stress regime holds for both regions, i.e., $\sigma_1 = S_{Hmax}$, $\sigma_2 = S_V$, $\sigma_3 = S_{Hmin}$. In the following, we keep the realistic principal stress magnitude given in Eq 1 and Eq 2 but change in our different scenarii the axes along which they operate. This way, we are able to investigate the effect of tectonic regimes while keeping realistic stress ratios. For the understanding of the results, the color code used in Eq. 1 and Eq. 2 is the same throughout the study. In order to allow the convergence of the 3D numerical calculations with this THM coupling, the application of the stresses is applied progressively from t = 0 yrs, until t = 10 yrs. The results are shown in steady-state, at 65 kyrs for the benchmark experiment, at 990 kyrs for the model where stresses are applied. The permeability k we will consider has been empirically demonstrated to be appropriate for fractured media (Lamur et al., 2017). It is written as:

$$\log k = (1 - \omega)\log k_i + \omega \log k_f$$

$$k_i = 4.979 \times 10^{-11} n^{3.11} \hspace{3cm} \text{Eq 3}$$

$$k_f = 1.143 \times 10^{-11} n^{0.64}$$

237
238   where ω representing the degree of rock fracturing, $\omega = 1$ for fully fractured rock, and $\omega = 0$
239   for fully intact rock. Here we take $\omega = 0.8$ corresponding to the significant fracturing degree of
240   the CFZ, interspersed with intact zones. n the initial porosity. Here $n = 0.05$ for intact rock, and
241    $n = 0.1$ for fractured rock. k_i (m^2) the permeability of intact rock, and k_f (m^2) the permeability
242   of fractured rock. The stress state of a fault can be qualitatively defined in terms of slip tendency
243   (Morris et al., 1996). In purely elastic domain and without dissipative phenomena the slip
244   tendency is an represents indicator (high/low general trend) to assess the stress variation on a
245   fault zone. More specifically, slip tendency indicates how critically stressed fault zones are, and
246   how easily they can be reactivated by, e.g., stimulation methods. Consequently, some
247   preferential flow paths may appear under the action of a given applied tectonic stress (Siler et al.,
248   2019). The slip tendency it is defined by:
249

250
$$T_S = \frac{\tau}{\sigma'_n} \qquad\qquad \text{Eq 4}$$

251

252   where τ is the shear stress and σ'_n the effective normal stress.
253
254
255
$$\sigma'_n = \sigma_n - (\alpha_B \times pf) \qquad\qquad \text{Eq 5}$$
256
257
258   where σ_n is the total normal stress; α_B Biot-Willis coefficient and pf fluid pressure.

259   **3 Results**

260   **3.1 Formation of a high temperature geothermal reservoir within a vertical fault zone with**
261   **no tectonic stresses, the benchmark experiment**

262   The numerical simulation without stress application shows an upward circulation at the
263   fault center and two downward circulations at the fault ends (Fig 1). As illustrated by colored
264   streamlines in Figure 1, these fluid circulations transfer heat by convection. Thermally induced
265   force is buoyancy are driving the flow. In a classical natural convection pattern, the hot fluid,
266   less dense, goes up to the surface, cools down, and its density increases, bringing back the fluid
267   down deeper in the fault.
268
269   Considering realistic physical conditions, no external heat source except a basal heat flux, and no
270   mechanical stress, this free convection generates a thermal disturbance of the environment and
271   localized the 150°C isotherm at 1.8 km depth, at the center of the fault. By comparison, in a
272   purely diffusive setting, we would reach 150°C at 5 km depth. Fluid velocities are of the order of
273   1×10^{-9} m.s^{-1} at the center of the fault and 20×10^{-9} m.s^{-1} at the ends of the fault. The higher
274   fluid velocities at the bottom center of the fault are responsible for slight increase in pressure
275   (white lines). This trend is already observed in other numerical TH modeling (Scott et al., 2017).

276   The temperature gradient at the center of the model is similar to typical temperature gradient in
277   geothermal reservoirs such as Soultz-sous-Forêts (Genter et al., 2010).

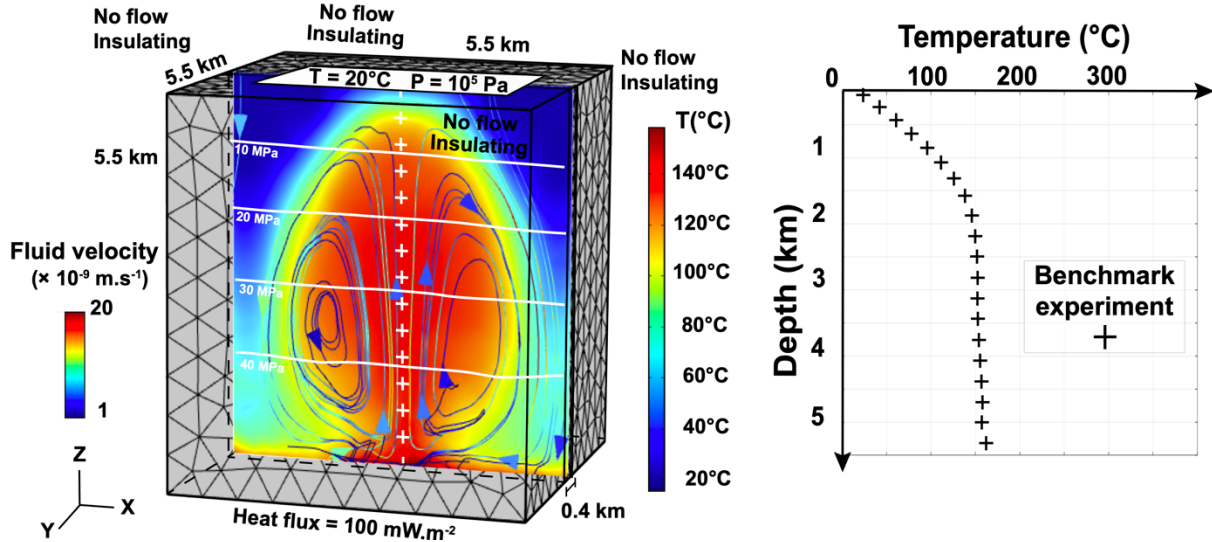## 3.2 Application of tectonic stresses

Figure 1 : Model setup, initial condition and results of the benchmark experiment (+) -without stress application-. Pressure (white contour), temperature (color patterns) and flow field (vectors) are displayed. The temperature profile is plotted against depth (right chart, dotted line). When free convection is established, the 150°C isotherm is located at 1.8 km depth. The benchmark experiment reaches the steady-state regime at 65 kyrs.

279   Figure 2 (with tectonic regimes written in red) corresponds to the high stress intensity application
280   (see the definition of high stress intensity in the method section, Eq 1). Figure 3 (with tectonic
281   regimes written in green) corresponds to the low stress intensity application (see the definition of
282   low stress intensity in the method section, Eq 2). Results are shown on vertical cross sections in
283   the fault, and on horizontal cross sections, at 2 km depth. For each tectonic regime that is
284   considered, the results show the temperature anomalies, the fluid flow pattern and the fluid
285   velocities. The results are different from the benchmark experiment (Fig 2 and 3).

3.2.1 Different Temperature Anomalies

287   Regardless of the considered tectonic regime, positive and negative temperature anomalies are
288   observed. They differ by their number, intensity and lateral extension.
289
290   **3.2.1.1** In extensional tectonic regime, two positive temperature anomalies are found (Fig 2 and
291   3). They are +55 °C in high stress intensity and +47 °C in low stress intensity. For both stress
292   intensities, the second temperature anomalies are less intense, + 10°C in high stress intensity, and
293   +7 °C in low stress intensity. For both stress intensities, a negative temperature anomaly at the
294   center of the fault is found. This anomaly is -60°C for the high stress intensity and -57°C for the
295   low stress intensity. For a high stress intensity, at 2 km depth, the horizontal cross-section shows
296   a negative temperature anomaly that reaches a maximum of -30°C. This anomaly covers a large

297 surface area of the fault. The positive temperature anomaly of +45°C occupies the remaining
298 space, but extends further into the basement. In the basement and up to the edge of the model, we
299 find a positive temperature anomaly of +20°C. For a low stress intensity, at 2 km depth, two
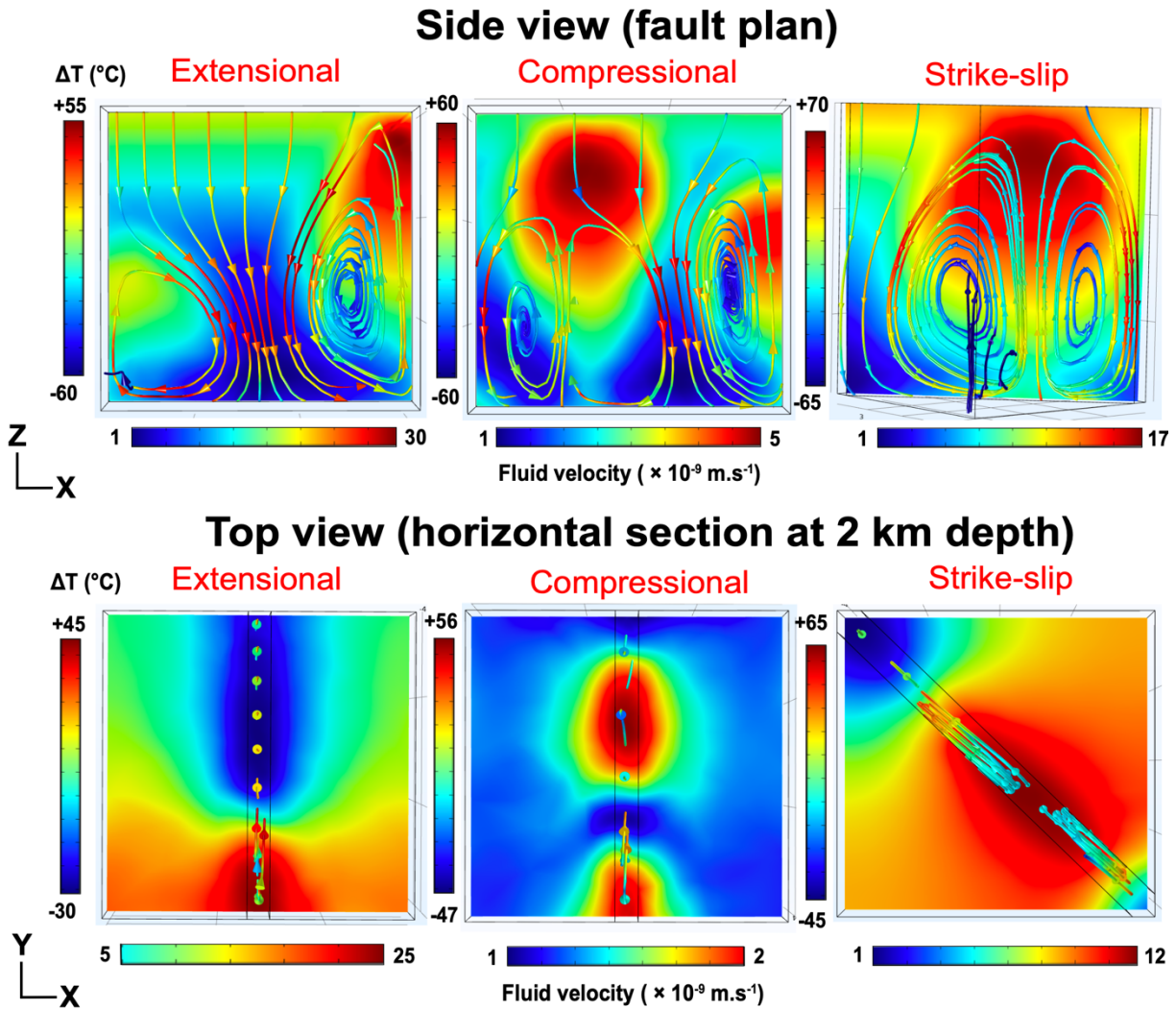300 positive temperature anomalies and one negative anomaly are observed.
301

Figure 2 : Results of numerical modeling after high stress intensity stresses application (in
red, see Eq 2). The results are shown in vertical section (Side View, located in the middle of
the fault) and in horizontal section, (Top view, located at 2 km depth). The scale of
temperature anomalies and fluid flow velocities is different according to the tectonic regimes.
For each regime, the maximum and minimum values of temperatures and fluid flow velocities
are indicated. Positive temperature anomalies are colored red, negative temperature anomalies
are colored blue. Fluid circulation is marked by the lines, the direction by the arrows. The
color of the lines corresponds to the fluid velocity. In red the velocity is the highest, in blue
the velocity is the lowest.

302 The first positive anomaly is +41 °C, the second has a value of +20 °C. This +20 °C anomaly
303 spreads more widely in the system whilst the +41 °C anomaly remains localized on the fault. The

304 negative anomaly located at the center of the fault is -37 °C and extends into the basement in the
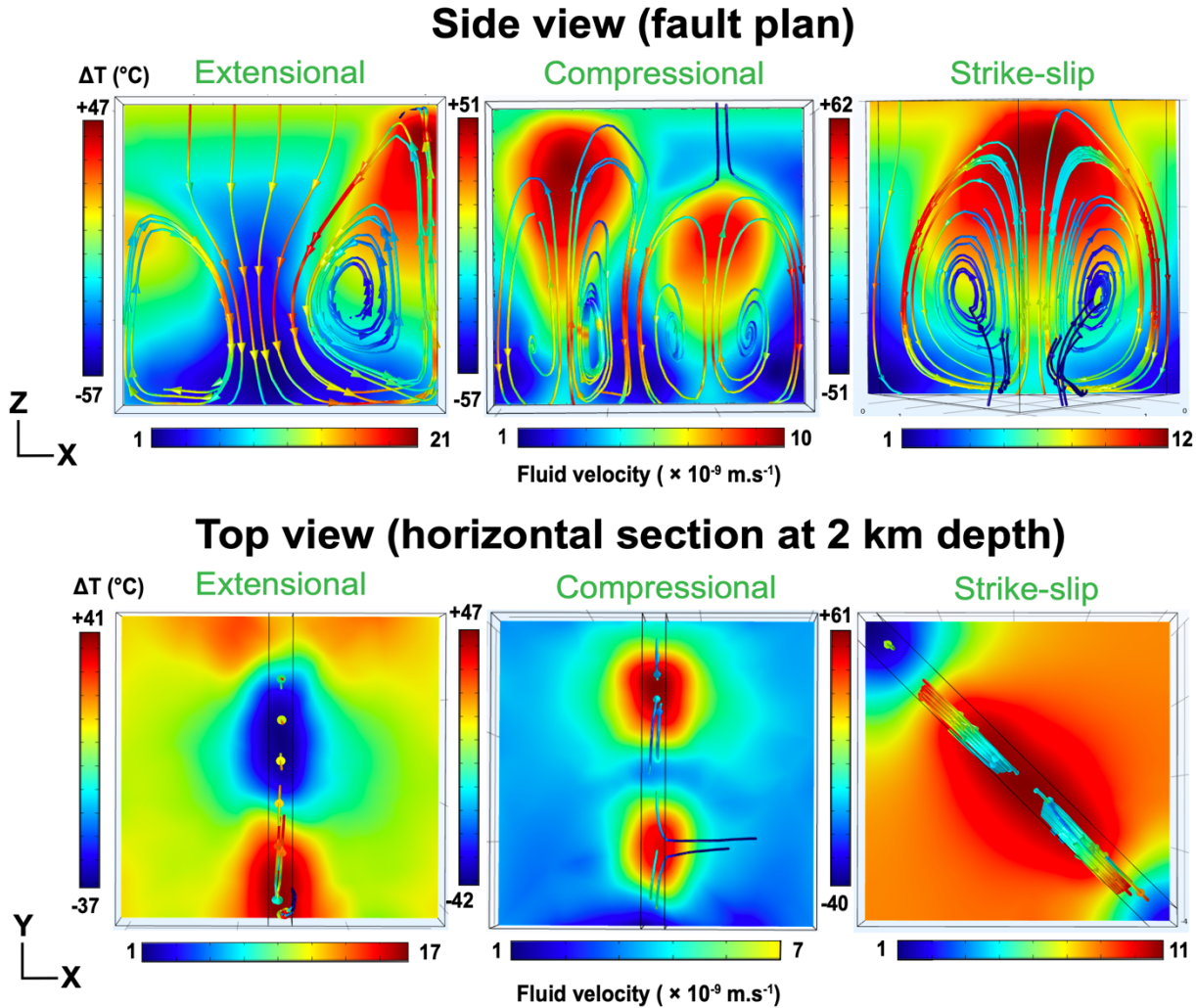305 same way as the positive +41 °C anomaly.
306

Figure 3 : Results of numerical modeling after low stress intensity application (in green, see Eq 1). The results are shown in vertical section (Side View, located in the middle of the fault) and in horizontal section, (Top view, located at 2 km depth). The scale of temperature anomalies and fluid flow velocities is different according to the tectonic regimes. For each regime, the maximum and minimum values of temperatures and fluid flow velocities are indicated. Positive temperature anomalies are colored red, negative temperature anomalies are colored blue. Fluid circulation is marked by the lines, the direction by the arrows. The color of the lines corresponds to the fluid velocity. In red the velocity is the highest, in blue the velocity is the lowest.

307

308 **3.2.1.2** In compressional tectonic regime, independently from the stress intensity, we find two
309 positive temperature anomalies. The value of the maximum temperature anomaly in high stress
310 intensity is +60 °C and in low intensity it is +51 °C. Depending on the stress intensity, these two

311   maximum values are spatially slightly shifted (Fig 2 and 3). The amplitudes of the second

312   temperature anomaly are +35°C and +40°C for low and high stress intensity, respectively. In the

313   horizontal cross-section, the two temperature anomalies are found for each intensity. In high

314   stress intensity the values of these two temperature anomalies are +56 °C and +47°C. In low stre

315   stress intensity the values are +47 °C and +35 °C. The lateral extension of these temperature

316   anomalies is limited. They are surrounded by negative temperature anomalies that locally reach -

317   47°C in high intensity and -42°C in low intensity. At a depth of 2 km, the positive temperature

318   anomalies are much less extended than in extensional tectonic or strike-slip regimes (see below).

319   **3.2.1.3** In strike-slip regimes and regardless of stress intensity applied (Fig 2 and 3), positive

320   temperature anomaly extends widely along the length of the fault, from the surface to 4.5 km

321   deep. The maximum positive temperature anomaly value is +70°C for the high stress intensity

322   (Fig 2), and +62°C for the low stress intensity (Fig 3). In horizontal cross-section, these

323   temperature anomalies spread largely beyond the fault. Temperature anomalies of + 25°C are

324   found in the basement, suggesting that in a strike-slip system, the positive temperature anomaly,

325   and independently from the stress intensity, represents an important volume. This heat

326   propagation is done by thermal diffusion from the fault center, where the temperature anomaly is

327   the most intense. Indeed, the larger the convection cell inside the fault, the wider the extent of the

328   diffusive perturbation. At 2 km depth, the maximum value of the temperature anomaly is +65 °C

329   for the high stress intensity, and +61 °C for the low stress intensity. Negative temperature

330   anomalies are present and localized at the extremities of the fault. They are -45°C for the high

331   stress intensity and -40°C for the low stress intensity.

332   To summarize, tectonic regimes influence the distribution and the amplitude of temperature

333   anomalies. Positive temperature anomalies are most intense in strike-slip, then in compression

334   and extension. The spatial extent of positive temperature anomalies is not identical for each

335   tectonic regime. In strike-slip, these anomalies are largely extended through the basement. This

336   lateral extension is less important in the extensive tectonic regime. Finally, in compressional

337   regime these anomalies are localized in the near vicinity of the fault. The tectonic regimes have

338   shown to play a key role in temperature, and this is clearly related to the different convective

339   patterns and fluid flow velocity, as described below.

340   3.2.2 Fluid flow pattern

341   **3.2.2.1** In extensional tectonic regimes, the fluid flow pattern is characterized by a downward

342   movement at the center of the fault and two upward movements at the ends of the fault (Fig 2

343   and 3). In high stress intensity the maximum fluid velocity is 30×10^{-9} m.s^{-1}, against 21×10^{-9}

344   m.s^{-1} in low stress intensity. The minimum fluid velocities are, for each intensity, 1×10-9 m.s^{-1}.

345   In horizontal cross-section, at 2 km depth, upward movements are localized at positive

346   temperature anomalies, while downward movements are localized at negative temperature

347   anomalies. In high stress intensity, the maximum fluid velocity is 25×10^{-9} m.s^{-1}, compared to 17

348   $\times 10^{-9}$ m.s^{-1} in low stress intensity. And the minimum fluid velocity is 5×10^{-9} m.s^{-1} in high

349   stress intensity, compared to 1×10^{-9} m.s^{-1} in low stress intensity.

350

351   **3.2.2.2** In compressional tectonic regimes, for each stress intensity, there is a slightly different

352   convective pattern. In high stress intensity, there are two upward and two downward movements

353   whereas in low stress intensity, there are two upward and three downward movements. The

354 maximum fluid velocity for high stress intensity is 5×10^{-9} m.s^{-1} and 10×10^{-9} m.s^{-1} for low
355 stress intensity. For this tectonic regime the maximum fluid velocity is present when the lowest
356 stress intensity is applied. In horizontal cross-section, at 2 km depth, and for high stress intensity
357 upward movements are localized where temperature anomalies are positive whereas downward
358 movements are localized where temperature anomalies are negative. The fluid velocity is
359 between 1 and 2×10^{-9} m.s^{-1}. In low stress intensity, the downward movements are localized at
360 the extremities and at the center of the fault. The upward movements are localized between each
361 downward movement. The maximum fluid velocity is 10×10^{-9} m.s^{-1} and the minimum is 1×10^{-9}
362 ^{9} m.s^{-1}. At a depth of 2 km, fluid velocities vary from 1 to 2×10^{-9} m.s^{-1}. Thus, fluid velocity
363 values in compressional regime are the lowest recorded.
364
365 **3.2.2.3** In the strike-slip tectonic regime, as for the benchmark experiment, the fluid flow pattern
366 is characterized by an upward movement at the center of the fault and two downward movements
367 at the ends of the fault (Fig 2 and Fig 3), as observed in the benchmark experiment. The fluid
368 velocity varies with stress intensity. In low stress intensity, the minimum fluid velocity is 1×10^{-9}
369 ^{9} m.s^{-1} and the maximum is 12×10^{-9} m.s^{-1} at the downward movements. In high stress intensity,
370 the minimum fluid velocity is 1×10^{-9} m.s^{-1} and the maximum is 17×10^{-9} m.s^{-1}.
371
372 With application of tectonic stresses; the fluid flow is different from the benchmark experiment,
373 with consequences on temperature anomalies. In the benchmark experiment, buoyancy is the
374 only driving force for fluid convection. Here, in presence of tectonic stresses, other forces seem
375 to influence the fluid flow.

376 **3.2.3 Lateral fluid pressure variation**

377
378 After stress application, the fluid pressure is different from the benchmark experiment, where
379 pressure is hydrostatic (Fig 4). Whatever the stress intensity applied, the experiment with
380 compressional and strike-slip tectonic regimes show fluid pressures higher than those in the
381 benchmark experiment, whereas, the extensional tectonic regime display fluid pressures lower
382 than those in the benchmark experiment. The fluid pressure varies between the basement and the
383 fault. This lateral variation differs according to the stress intensity applied.
384
385 In each of these cases, the tectonic regimes and the stress intensity generate lateral fluid pressure
386 variation between the fault and the basement. In high stress intensity, and for the same horizontal
387 distance, these lateral pressure differences are 1.5 MPa, 0.45 MPa, and 0.97 MPa for
388 compressional, strike-slip, and extensional tectonic regimes, respectively. In low stress intensity
389 the lateral pressure differences are 1.35 MPa, 0.3 MPa and 0.91 MPa for compressional, strike-
390 slip, and extensional tectonic regimes (respectively). These lateral fluid pressure differences
391 drive the fluids from the high-pressure zones (i.e. basement), to the low-pressure zone (i.e. fault).
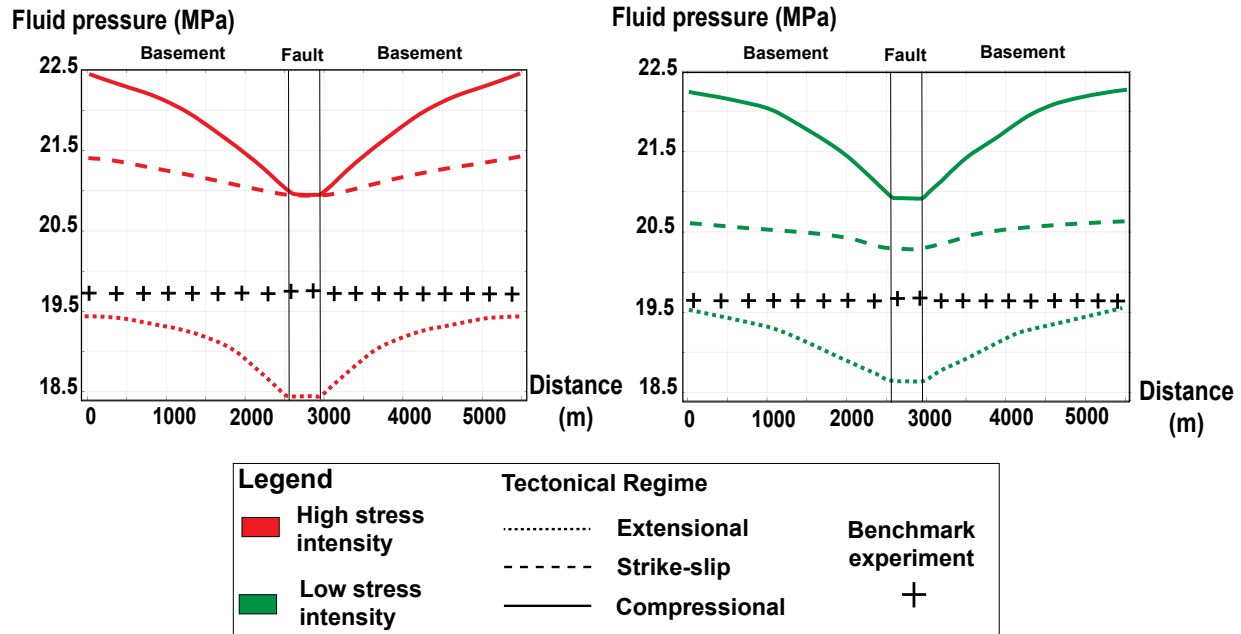392
393
394
395

Figure 4 : Graphs representing the lateral fluid pressure in high stress intensity application (in red), and low stress intensity application (in green). The fluid pressure of the benchmark experiment is indicated (+). With stresses application, the fluid pressure is different than the benchmark experiment. The lateral fluid pressure variation depends on the tectonic regime and stress intensity.

396

3.2.4 What effect(s) on the onset of the positive temperature ?

398

399   The regional mechanical stresses imposed a pressure distribution that will interact with buoyancy
400   forces responsible for free convection patterns. The lateral fluid pressure differences bring the
401   fluid from the zones of high pressure to those of low pressure. However, the time needed to set
402   up this temperature anomaly appears to vary, as show in Figure 5.

403
404
405
406
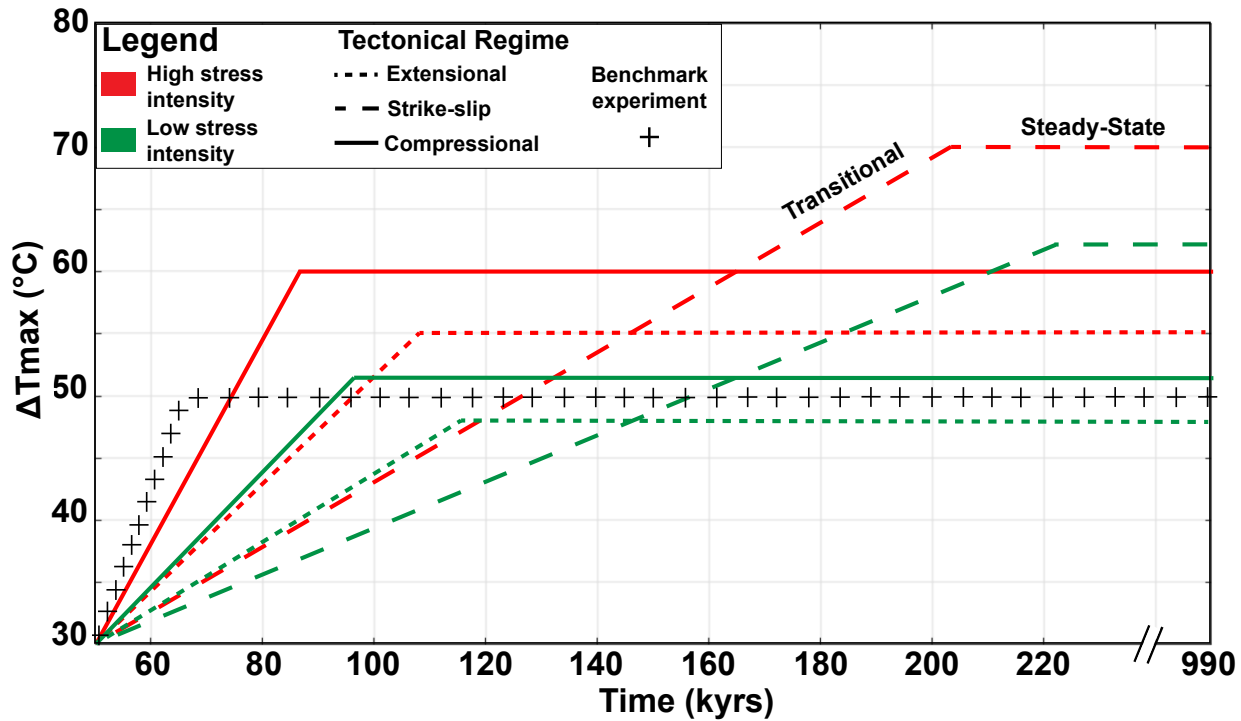407
408
409
410
411
412
413
414
415

Figure 5 : Time required to reach the steady-state temperature anomalies, depending on the tectonic regimes and the applied stress intensities. The color code and patterns are the same as those used in the previous figures.

416

417 Considering the compressional tectonic regime (solid line), the time needed to reach a steady-
418 state regime in high stress intensity is 85 kyrs, while it is 95 kyrs in low stress intensity. This
419 difference is observed for each regime, so that the stress intensity has a role in the setting up
420 convection. The high stress intensity allows bringing the fluid more quickly to the zone of high
421 permeability, and low fluid pressure. In this way, the compressional regime, which has the
422 highest lateral fluid pressure difference, reaches the steady-state more quickly than the other
423 tectonic regimes. The lowest lateral fluid pressure difference is recorded for the strike-slip
424 regime. The strike-slip regime reaches the steady-state regime at 203 kyrs for high stress
425 intensity and 223 kyrs for low stress intensity.

426

427 In a geothermal exploration context, these numerical calculations show that in a strike-slip
428 tectonic regime the temperature anomalies should be more intense than in a compressive or
429 extensive regime, but that the onset is the most delayed with respect to the benchmark case.
430 The benchmark experiment reaches the steady-state regime as early as 65 kyrs, and finally the
431 additional stress input may increase the time to reach a steady-state in situ. The differences
432 observed on the different tectonic regimes is consistent with the differences observed on the
433 lateral fluid pressure between the fault and the basement. However, this does not allow to explain
434 the different fluid velocities observed (Fig 2 and 3), and the mechanical behavior of the
435 basement-fault system after stress application.

436

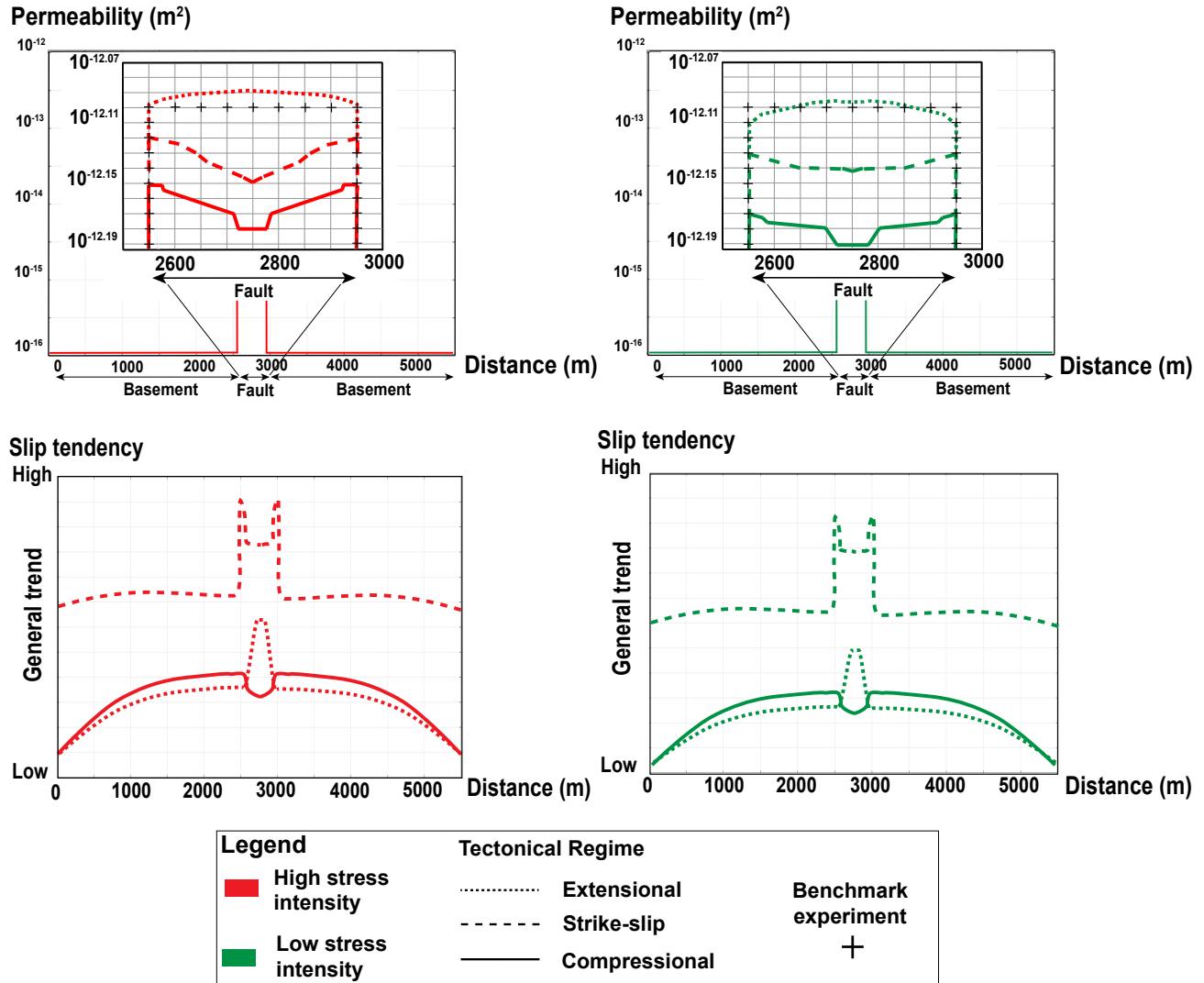**437   3.2.5 Permeability and slip tendency variation**

Figure 6 : Graphs representing the permeability and the slip tendency in high stress intensity application (in red), and low stress intensity application (in green). The permeability of the benchmark experiment is indicated (+).

438

439   In the fault, very small permeability variations are observed as a function of stress intensity and
440   tectonic regime (Fig 6). In high stress intensity, the permeability values in the center of the fault
441   are $10^{-12.09}$, $10^{-12.15}$, $10{-}12.18$ m2, for extensional, strike-slip and compressional tectonic regimes,
442   respectively. In low stress intensity, the permeability values are $10^{-12.09}$, $10^{-12.14}$, $10^{-12.19}$ m^2, for
443   extensional, strike-slip and compressional tectonic regimes, respectively. The effect of stress
444   intensity on permeability remains negligible. For example, considering the compressional
445   tectonic regime, the difference between high and low stress intensity is to 2.3 %.
446   To understand if these small variations in permeability between the tectonic regimes can explain
447   the different convective patterns previously described, runs were performed considering the two

448   extreme values of permeability obtained: $10^{-12.09}$ and $10^{-12.19}$ m^2 (for more details see Appendix
449   2). The general thermal distribution of the system remains identical.

451   We note a consistency between the values of fluid velocities and permeability values. Indeed, the
452   fluid velocities are the most important for the highest permeability, and the least important for
453   the lowest permeability. Once the stresses are applied, the permeability are slightly different
454   from the benchmark experiment, and control the fluid velocity.

456   The slip tendency is calculated and plotted for each tectonic regime and stress intensity applied
457   (Fig 6). The global general trend is higher in high stress intensity than in low stress intensity
458   applied. The results show a distinctive variation in the fault and in the basement for each tectonic
459   regime. Regardless of the stress intensity applied, the slip tendency in a strike-slip tectonic
460   regime is the highest, since it is more critically stressed. In the strike-slip regime, the slip
461   tendency increases slightly from the edge of the basement to the level of the fault zone. At the
462   edge of the fault, the slip tendency increases significantly. In the middle of the fault, the slip
463   tendency slightly decreases. This evolution is the same independently from the stress intensity
464   applied.

466   In compressional and extensional regimes, the trend from the edges of the basement to the fault
467   increases similarly. This increase is slightly greater in compression than in extension. At the edge
468   of the fault the general trend is the same. In compression the slip tendency decreases, and in
469   extension it increases. In extension the middle of the fault is less critically stressed than in
470   compression. Independently from the intensity of the stress this evolution is the same. Of the
471   three tectonic regimes tested, the strike-slip regime is the most critically stressed. The general
472   trend shows that it is at the interface between the basement and the fault that the trend is most
473   important. This result illustrates the heterogeneity of the mechanical parameters incorporated in
474   the numerical model, and also show that the role of the stress intensity on the range of values
475   tested will not drastically change the mechanical response of the basement-fault system.

4 Discussion and Conclusion

479   The presence of fluids and a sufficiently high permeability are two factors to allow the
480   development of a geothermal resource, from a natural geothermal flux. Considering a simplified
481   geometry, but realistic physical properties (pressure and temperature dependent fluid density,
482   temperature-dependent fluid viscosity), our 3D TH and 3D THM numerical modeling show that
483   in a basement domain, CFZs allow hot fluids to rise to economically viable depths. The
484   comparison of numerical models with and without tectonic stresses highlight the non-negligible
485   role of tectonic regime on the spatial distribution of positive temperature anomalies.
486   Without stress application, the benchmark experiment shows that an upward movement at the
487   center of the fault and brings a temperature of 150 °C at 1.8 km depth (Fig 1). Two downward
488   movements are located at the ends of the fault. This convective pattern has already been
489   observed in 2D and 3D TH numerical modeling of fault zones in the crustal domain (Wanner et
490   al., 2019; Guillou-Frottier et al., 2020) and was called "bulb-like" convective pattern. This
491   particular shape is favored because hot fluids have less resistance when flowing upwards
492   (viscosity is smaller at high temperature) and can localize temperature anomalies also in the

493 basement. With a flat topography and without metamorphic devolatilization and/or magmatic
494 fluid production that might change fluid pressure (Nur and Walder, 1990), fluid circulation is
495 only driven by the buoyancy force. With tectonic regimes application, we have seen that other
496 forces are added and modify the fluid circulation.
497
498 Considering the experiments where tectonic regimes are accounted for, the obtained results are
499 different from the benchmark experiment (Fig 2 and Fig 3). This highlights the key role of the
500 relationship between tectonic settings and fluid flow. In our results, the stress intensity parameter
501 does not change the general dynamics of convective patterns between two identical regimes.
502 Considering a sensitivity study on a large Pontgibaud Crustal Fault Zone (French Massif
503 Central), where the stresses boundary magnitudes are tested while holding their directions, a shift
504 from one convective pattern to another would occur for a variation of approximately 40 MPa in
505 the maximum horizontal stress magnitude (Duwiquet et al., 2021). For this last example and in
506 the light of the observations made in this study, it could be possible that another force than the
507 buoyancy, influences fluid circulation. In this study the stress intensity applied is not a factor
508 influencing the convection pattern. However, the stress intensity has a role in the time to reach
509 the steady-state. Indeed, the steady-state is reached faster when the most intense stresses are
510 applied (Fig 5), and this was not explored in the Duwiquet et al. (2021) study. Moreover, the role
511 of tectonics on the direction of fluid flow has been highlighted. Considering a numerical
512 approach, studies have shown that in compression, upward fluid movements are favored (Upton,
513 1998), whereas in extension, downward fluid movements are favored (Cui et al., 2012). Here we
514 could see that the different tectonic regimes will have a role in the onset of convection. This
515 element also explains the final results observed.
516
517 These numerical models show that the tested tectonic regimes have an influence on fluid
518 pressure variation. The poroelastic assumption describes the interaction of fluids and
519 deformation in porous media. Compressional, extensional, and strike-slip tectonic regimes
520 induce variable fluid pressures for each case. The incorporation of heterogeneous mechanical
521 parameters between the fault and the basement (see Table 1) leads to a different mechanical
522 response and thus to a heterogeneous variation of the fluid pressure between the fault and the
523 basement (see Fig 4). This lateral fluid pressure difference drives the fluids from the high-
524 pressure zones to the low-pressure zones. This effect is facilitated by higher permeability values
525 in the fault than in the basement.
526
527 This force, which drives fluids from high pressure zones to low pressure zones is similar to the
528 effects of topography on fluid flow (Forster and Smith, 1989; López and Smith, 1995). This
529 poroelasticity driven force will therefore influence the initial fluid motions (downward and
530 upward movement) and thus the time required for the steady-state temperature anomaly to
531 develop. Considering a TH coupling, the fluid circulation in the benchmark experiment is driven
532 by free convection. Considering three different tectonic regimes with the same TH coupling, the
533 fluid circulation is the result of an interplay between forced and free convection. These changes
534 are not related to boundary conditions, but to the tectonic regimes themselves. Forced convection
535 is referred to as stress induced convection.
536
537 After stress applications, the permeability values obtained are consistent with fractured and
538 altered granitic environment (Sardini et al., 1997; Duwiquet et al., 2019; 2021; Gomila et al.,

539 2021). This should be sufficient to allow fluids to flow by buoyancy forces and transfer heat by
540 free convection. However, between tectonic regimes, the difference in permeability cannot
541 explain convective pattern variability results. Nevertheless, these small permeability variations
542 influence the velocities of fluid flow. The fluid velocity decreases with a permeability decrease
543 (see Fig 2, 3, and 6). Actually, the positive temperature anomalies in the compression and
544 extensional regime model remain centered on the fault compared to the extensional and strike-
545 slip tectonic regimes. Therefore, other processes must limit the development of temperature
546 anomalies in compressional regime. By concentrating the flow of fluids on limited spaces, the
547 poroelasticity driven force could have the effect of spatially concentrating temperature anomalies
548 when the difference between the fluid pressure of the basement and the fault is large.
549
550 For geothermal exploration, slip tendency analyses can be used to target favorable zones for
551 natural fluid flow and future enhancement by fault reactivation (Barton et al., 1995; Morris et al.,
552 1996; Ito and Zoback, 2000). Our results show that the strike-slip regime would be the most
553 favorable to allow fluid flow. The occurrence of geothermal reservoirs in such contexts is
554 already known, Alpine Fault, New Zealand (Boulton et al., 2012), the Geysers (Altmann et al.,
555 2013). In the light of our results, an exploratory phase on the geothermal potential of fault zones
556 could further consider strike-slip faulted as interesting targets for geothermal power system.
557
558 If slip tendency can be used as a potential qualitative indicator in purely elastic models, a more
559 accurate interpretation would require incorporating dissipative mechanical behaviors such as,
560 e.g., Mohr-Coulomb elasto-plastic law, which would allow to quantify the variation in slip
561 tendency. By considering irreversible mechanical processes, including dilation (opening under
562 shearing) and fracturing (increase of pore space/fractures), the best favorability of strike-slip
563 regime towards convection is expected to be emphasized.
564
565 We used an idealized geometry with single, vertical fault zone. The linear stress boundary
566 conditions hence give rather homogeneous stress ratios and states along the fault. In natural
567 systems, the network of variously oriented and dipping fault zones brings heterogeneous stress
568 states, even along each fault zone taken separately. Still, and recalling that the aim of our study is
569 to better understand the setup conditions of convection cells, the results already allow us to
570 highlight the complex impact of mechanics over convection patterns. Among others, our
571 conclusions tend to show that within a complex fault zone network, fault zones undergoing
572 strike-slip conditions might be the ones to be preferably explored.
573
574 These fundamental results are generally applicable in nature to any facture rock that may contain
575 fluids, gas or oil in its pores, in basement geological context. However, our results do not take
576 into account fundamental aspects such as the consideration of more complex rheology, to start
577 with plastic phenomena. The effects of fault intersections, precipitation and dissolution of
578 mineral phases, and fluid composition were also not taken into account. The dependence of
579 permeability on all of these phenomena should probably generate permeability anisotropy. The
580 development of this anisotropy can cause a change in the intrinsic properties of the geothermal
581 reservoir and induce a change in the heat transfer mode (Sun et al., 2017). In cases where fluid
582 flow is important (i.e. areas of high permeability) the permeability can take a particular geometry
583 minimizing the resistance to flow and then optimizing fluid flow (Bejan and Lorente, 2011).

584 Fluid salinity could also play an important role, but effects would be marked above 400°C
585 (Driesner, 2007), which is beyond our modeled temperatures.
586
587 Geothermal energy can become a major asset for the transition to low-carbon energy sources. Its
588 development requires, prior to exploration, comprehensive understanding of limiting and
589 enabling factors controlling fluid flow and the location of temperature anomalies (Jolie et al.,
590 2021). Our numerical results show that the poroelasticity driven force provoked by the tectonic
591 regimes causes lateral fluid pressure variation, allowing for the more or less rapid development
592 of the temperature anomaly, by mixed, free and forced convection. For example, strike-slip
593 tectonic regimes would have the largest temperature anomalies, but would take the longest time
594 to set up.
595
596 Overall, this work suggests that anomalously permeable zone, like CFZ, with no external heat
597 source, have significant energy potential. The exploration of the vertical Crustal Fault Zones in
598 strike-slip stress regime, could accelerate the transition to low-carbon, renewable and climate-
599 neutral energy. Studies have already shown that major strike-slip fault zones localize porosity
600 and permeability even beyond the BDT (Faulkner et al., 2010; Cao and Neubauer, 2016). Our
601 study confirms that this tectonic regime seems to favor higher thermal anomalies than
602 compressional tectonics.
603
604 The complex nature of the processes occurring during the development of a geothermal resource
605 within a CFZ makes it an environment that requires a state-of-the-art numerical analysis of the
606 process that can control the fluid circulation. Such fully coupled analysis will help exploration
607 phases and ultimately promote the development of this renewable energy, not only in
608 anomalously hot areas, but in anomalously permeable areas, and thus promote the development
609 of this climate-neutral energy.

610 **References**

611
612 Altmann, J. B., Heidbach, O., & Gritto, R. (2013). Relative importance of processes leading to
613 stress changes in the Geysers geothermal area. *In Proceedings of thirty-eighth workshop on*
614 *geothermal reservoir engineering.*
615
616 Anderson, E. M. (1905). The dynamics of faulting. *Transactions of the Edinburgh Geological*
617 *Society*. 8(3), 387- 402. https://doi.org/10.1144/transed.8.3.387.
618
619 Barton, C. A., Zoback, M. D., & Moos, D. (1995). Fluid flow along potentially active faults in
620 crystalline rock. *Geology*. 23(8), 683-686. https://doi.org/10.1130/0091-
621 7613(1995)023<0683:FFAPAF>2.3.CO;2
622
623 Bejan, A., & Lorente, S. (2011) The constructal law and the evolution of design in
624 nature. *Physics of life Reviews*, 8(3), 209-240. https://doi.org/10.1016/j.plrev.2011.05.010.
625
626 Bethke, C. M. (1985). A numerical model of compaction-driven groundwater flow and heat
627 transfer and its application to the paleohydrology of intracratonic sedimentary basins. *Journal of*

628 *Geophysical Research: Solid Earth*. 90(B8), 6817-6828.
629 https://doi.org/10.1029/JB090iB08p06817
630

631 Ben-Zion, Y., & Rovelli, A. Properties and Processes of Crustal Fault Zones: Volume I. *Pure*
632 *and Applied Geophysics*. 171(11), 2863-2865 (2014).
633 https://doi.org/10.1007/s00024-014-0943-3
634

635 Cappa, F., & Rutqvist, J. (2011). Impact of CO2 geological sequestration on the nucleation of
636 earthquakes. *Geophysical Research Letters*. 38(17). https://doi.org/10.1029/2011GL048487.
637

638 Cao, S., & Neubauer, F. (2016). Deep crustal expressions of exhumed strike-slip fault systems:
639 Shear zone initiation on rheological boundaries. *Earth-Science Reviews*. 162, 155-176.
640 https://doi.org/10.1016/j.earscirev.2016.09.010
641

642 Cornet, F. H., & Burlet, D. (1992). Stress field determinations in France by hydraulic tests in
643 boreholes. *Journal of Geophysical Research: Solid Earth*. 97(B8), 11829-11849.
644 https://doi.org/10.1029/90JB02638.
645

646 Cox, S. F. (2005). Coupling between deformation, fluid pressures, and fluid flow in ore-
647 producing hydrothermal systems at depth in the crust. *Economic Geology*. 100, 39-75.
648

649 Cox, S. F. (1999). Deformational controls on the dynamics of fluid flow in mesothermal gold
650 systems. *Geological Society, London, Special Publications*. 155(1), 123-140.
651 https://doi.org/10.1144/GSL.SP.1999.155.01.10
652

653 Cui, T., Yang, J., & Samson, I. M. (2012).Tectonic deformation and fluid flow: implications for
654 the formation of unconformity-related uranium deposits. *Economic Geology*. 107(1), 147-163.
655 https://doi.org/10.2113/econgeo.107.1.147.
656

657 Deichmann, N., and Giardini, D. (2009). Earthquakes induced by the stimulation of an enhanced
658 geothermal system below Basel (Switzerland). *Seismological Research Letters*. 80(5), 784-798.
659 https://doi.org/10.1785/gssrl.80.5.784.
660

661 Driesner, T. (2007) The system H2O–NaCl. Part II: Correlations for molar volume, enthalpy, and
662 isobaric heat capacity from 0 to 1000 C, 1 to 5000 bar, and 0 to 1 XNaCl. *Geochimica et*
663 *Cosmochimica Acta*. 71(20), 4902-4919. https://doi.org/10.1016/j.gca.2007.05.026.
664

665 Duwiquet, H., Arbaret, L., Guillou-Frottier, L., Heap, M. J., Bellanger, M. (2019). On the
666 geothermal potential of crustal fault zones: a case study from the Pontgibaud area (French Massif
667 Central, France). *Geothermal Energy*. 7(1), 1-29. https://doi.org/10.1186/s40517-019-0150-7.
668

669 Duwiquet, H., Guillou-Frottier, L., Arbaret, L., Bellanger, M., Guillon, T., Heap, M. J. (2021)
670 Crustal Fault Zones (CFZ) as Geothermal Power Systems: A Preliminary 3D THM Model
671 Constrained by a Multidisciplinary Approach. *Geofluids*. 2021.
672 https://doi.org/10.1155/2021/8855632
673

674 Duwiquet, H., Guillou-Frottier, L., Arbaret, L., Bellanger, M., Guillon, T., Heap, M. J Crustal
675 Fault Zones (CFZ) as Geothermal Power Systems: 3D Variation of Permeability and Related
676 Processes. In Stanford Geothermal Workshop. (2021, February)

678 Eldursi, K., Chi, G., Bethune, K., Li, Z., Ledru, P., & Quirt, D. (2020). New insights from 2-and
679 3-D numerical modelling on fluid flow mechanisms and geological factors responsible for the
680 formation of the world-class Cigar Lake uranium deposit, eastern Athabasca Basin,
681 Canada. *Mineralium Deposita*. 1-24. https://doi.org/10.1007/s00126-020-00979-5.

683 Evans, K. F. et al. (2005). Microseismicity and permeability enhancement of hydrogeologic
684 structures during massive fluid injections into granite at 3 km depth at the Soultz HDR site.
685 *Geophysical Journal International*. 160(1), 388-412. https://doi.org/10.1111/j.1365-
686 246X.2004.02474.x.

688 Famin, V., Philippot, P., Jolivet, L., & Agard, P. (2004). Evolution of hydrothermal regime along
689 a crustal shear zone, Tinos Island, Greece. *Tectonics*. 23(5).
690 https://doi.org/10.1029/2003TC001509.

692 Faulkner, D. R., Lewis, A. C., & Rutter, E. H. (2003). On the internal structure and mechanics of
693 large strike-slip fault zones: field observations of the Carboneras fault in southeastern
694 Spain. *Tectonophysics*, 367(3-4), 235-251.
695 https://doi.org/10.1016/S0040-1951(03)00134-3

697 Faulkner, D. R., Jackson, C. A. L., Lunn, R. J., Schlische, R. W., Shipton, Z. K., Wibberley, C.
698 A. J., & Withjack, M. O. (2010). A review of recent developments concerning the structure,
699 mechanics and fluid flow properties of fault zones. *Journal of Structural Geology*. **32(11)**, 1557-
700 1575. https://doi.org/10.1016/j.jsg.2010.06.009

702 Forster, C., & Smith, L. (1989). The influence of groundwater flow on thermal regimes in
703 mountainous terrain: A model study. *Journal of Geophysical Research: Solid Earth*. 94(B7),
704 9439-9451. https://doi.org/10.1029/JB094iB07p09439.

706 Gomila, R., Arancibia, G., Nehler, M., Bracke, R., Morata, D., & Cembrano, J. (2021).
707 Quantitative anisotropies of palaeopermeability in a strike-slip fault damage zone: Insights from
708 micro-CT analysis and numerical simulations. *Tectonophysics*, 228873.
709 https://doi.org/10.1016/j.tecto.2021.228873

711 Genter, A., Evans, K., Cuenot, N., Fritsch, D., Sanjuan, B. (2010) Contribution of the exploration
712 of deep crystalline fractured reservoir of Soultz to the knowledge of enhanced geothermal
713 systems (EGS). *Comptes Rendus Geoscience*. 342(7-8), 502-516.
714 https://doi.org/10.1016/j.crte.2010.01.006

716 Gleeson, T., & Ingebritsen, S. (Eds.). Crustal permeability. John Wiley & Sons. (2016).

718 Glover, P. W. J., Matsuki, K., Hikima, R., & Hayashi, K. (1998). Fluid flow in synthetic rough
719 fractures and application to the Hachimantai geothermal hot dry rock test site. *Journal of*
720 *Geophysical Research: Solid Earth*. 103(B5), 9621-9635. https://doi.org/10.1029/97JB01613
721
722 Grawinkel, A., & Stöckhert, B. (1997). Hydrostatic pore fluid pressure to 9 km depth-Fluid
723 inclusion evidence from the KTB deep drill hole. *Geophysical Research Letters*. 24(24), 3273-
724 3276. https://doi.org/10.1029/97GL03309
725
726 Guillou-Frottier, L., Carré, C., Bourgine, B., Bouchot, V., & Genter, A. (2013). Structure of
727 hydrothermal convection in the Upper Rhine Graben as inferred from corrected temperature data
728 and basin-scale numerical models. *Journal of Volcanology and Geothermal Research*. 256, 29-
729 49. https://doi.org/10.1016/j.jvolgeores.2013.02.008
730
731 Guillou-Frottier. L., Duwiquet, H., Launay, G., Taillefer, A., Roche, V., & Link, G. (2020). On
732 the morphology and amplitude of 2D and 3D thermal anomalies induced by buoyancy-driven
733 flow within and around fault zones. *Solid Earth*. 11(4), 1571-1595. https://doi.org/10.5194/se-11-
734 1571-2020.
735
736 Heap, M. J., et al. (2020). Towards more realistic values of elastic moduli for volcano
737 modelling. *Journal of Volcanology and Geothermal Research*. 390, 10668.
738 https://doi.org/10.1016/j.jvolgeores.2019.106684.
739
740 Horton, C. W., & Rogers Jr, F. T. (1945). Convection currents in a porous medium. *Journal of*
741 *Applied Physics*. 16(6), 367-370. https://doi.org/10.1063/1.1707601.
742
743 Horne, R. N. (1979). Three-dimensional natural convection in a confined porous medium heated
744 from below. *Journal of Fluid Mechanics*. 92(4), 751-766.
745
746 Ito, T., & Zoback, M. D. (2000). Fracture permeability and in situ stress to 7 km depth in the
747 KTB scientific drillhole. *Geophysical Research Letters*. 27(7), 1045-1048.
748 https://doi.org/10.1029/1999GL011068
749
750 Katto, Y., & Masuoka, T. (1967). Criterion for the onset of convective flow in a fluid in a porous
751 medium. *International Journal of Heat and Mass Transfer*. 10(3), 297-309.
752 https://doi.org/10.1016/0017-9310(67)90147-0.
753
754 Kozlovsky, Y. (1984). The World's Deepest Well. Scientific American, 251(6), 98-105. from
755 http://www.jstor.org/stable/24969503
756
757 Kwiatek, G., Bohnhoff, M., Dresen, G., Schulze, A., Schulte, T., Zimmermann, G., & Huenges,
758 E. (2010). Microseismicity induced during fluid-injection: A case study from the geothermal site
759 at Groß Schönebeck, North German Basin. Acta Geophysica. 58(6), 995-1020.
760 https://doi.org/10.2478/s11600-010-0032-7
761

762 Lamur, A., Kendrick, J. E., Eggertsson, G. H., Wall, R. J., Ashworth, J. D., & Lavallée, Y.
763 (2017). The permeability of fractured rocks in pressurised volcanic and geothermal
764 systems. *Scientific reports*. 7(1), 1-9. https://doi.org/10.1038/s41598-017-05460-4.
765

766 Ledingham, P., Cotton, L., & Law, R. (2019). The united downs deep geothermal power
767 project. *Proc. 44th Work. Geotherm. Reserv. Eng*, 1-11.
768

769 López, D. L., & Smith, L. (1995).Fluid flow in fault zones: analysis of the interplay of
770 convective circulation and topographically driven groundwater flow. *Water resources
771 research*. 31(6), 1489-1503. https://doi.org/10.1029/95WR00422.
772

773 Liang, X., Xu, T., Feng, B., & Jiang, Z. (2018). Optimization of heat extraction strategies in
774 fault-controlled hydro-geothermal reservoirs. *Energy*. 164, 853-870.
775 https://doi.org/10.1016/j.renene.2019.02.070
776

777 Magri, F., Cacace, M., Fischer, T., Kolditz, O., Wang, W., & Watanabe, N. (2017).Thermal
778 convection of viscous fluids in a faulted system: 3D benchmark for numerical codes. Energy
779 Procedia. 125, 310-317. https://doi.org/10.1016/j.egypro.2017.08.204
780

781 McLellan, J. G., Oliver, N. H. S., & Schaubs, P. M. (2004). Fluid flow in extensional
782 environments; numerical modelling with an application to Hamersley iron ores. *Journal of
783 Structural Geology*. 26(6-7), 1157-1171. https://doi.org/10.1016/j.jsg.2003.11.015
784

785 Morris, A., Ferrill, D. A., Henderson, D. B. (1996). Slip-tendency analysis and fault
786 reactivation. *Geology*. 24(3), 275-278. https://doi.org/10.1130/0091-
787 7613(1996)024<0275:STAAFR>2.3.CO;2
788

789 O'Sullivan, M. J., Pruess, K., & Lippmann, M. J. (2001) State of the art of geothermal reservoir
790 simulation. *Geothermics*. 30(4), 395-429. https://doi.org/10.1016/S0375-6505(01)00005-0.
791

792 Ord, A., & Oliver, N. H. S. (1997) Mechanical controls on fluid flow during regional
793 metamorphism: some numerical models. *Journal of Metamorphic Geology*. 15(3), 345-359.
794 https://doi.org/10.1111/j.1525-1314.1997.00030.x
795

796 Parisio, F., Vilarrasa, V., Wang, W., Kolditz, O., Nagel, T. (2019) The risks of long-term re-
797 injection in supercritical geothermal systems. *Nature communications*. 10(1), 1-11.
798 https://doi.org/10.1038/s41467-019-12146-0
799

800 Paulillo, A., Cotton, L., Law, R., Striolo, A., & Lettieri, P. (2020). Geothermal energy in the UK:
801 The life-cycle environmental impacts of electricity production from the United Downs Deep
802 Geothermal Power project. *Journal of Cleaner Production*, 249, 119410.
803

804 Phillips, W. J. (1972). Hydraulic fracturing and mineralization. *Journal of the Geological
805 Society*. 128(4), 337-359.
806

807   Rowland, J. V., & Sibson, R. H. (2004). Structural controls on hydrothermal flow in a segmented
808   rift system, Taupo Volcanic Zone, New Zealand. *Geofluids*. 4(4), 259-283.
809   https://doi.org/10.1111/j.1468-8123.2004.00091.x

810

811   Saevarsdottir, G., Tao, P. C., Stefansson, H., & Harvey, W. (2014). Potential use of geothermal
812   energy sources for the production of lithium-ion batteries. *Renewable energy*. 61, 17-22.
813   https://doi.org/10.1016/j.renene.2012.04.028

814

815   Sardini, P., Ledésert, B., & Touchard, G. (1997). Quantification of microscopic porous networks
816   by image analysis and measurements of permeability in the Soultz-sous-Forêts granite (Alsace,
817   France). *In Fluid flow and Transport in rocks*. 171-189. https://doi.org/10.1007/978-94-009-
818   1533-6_10

819

820   Scott, S., Driesner, T., & Weis, P. (2017). Boiling and condensation of saline geothermal fluids
821   above magmatic intrusions. *Geophysical Research Letters*. 44(4), 1696-1705.
822   https://doi.org/10.1002/2016GL071891.

823

824   Sibson, R. H. (1987). Earthquake rupturing as a mineralizing agent in hydrothermal
825   systems. *Geology*. 15(8), 701-704. https://doi.org/10.1130/0091-
826   7613(1987)15<701:ERAAMA>2.0.CO;2

827

828   Siebenaller, L. et al. (2013). Fluid record of rock exhumation across the brittle–ductile transition
829   during formation of a Metamorphic Core Complex (Naxos Island, Cyclades, Greece). *Journal of
830   Metamorphic Geology*. 31(3), 313-338. https://doi.org/10.1111/jmg.12023

831

832   Siler, D. L. Faulds, J. E., Hinz, N. H., Dering, G. M., Edwards, J. H., & Mayhew, B. (2019).
833   Three-dimensional geologic mapping to assess geothermal potential: examples from Nevada and
834   Oregon. *Geothermal Energy*. 7(1), 1-32. https://doi.org/10.1186/s40517-018-0117-0.

835

836   Sun, Z. X. et al. (2017). Numerical simulation of the heat extraction in EGS with thermal-
837   hydraulic-mechanical coupling method based on discrete fractures model. *Energy*. 120, 20-33.
838   https://doi.org/10.1016/j.energy.2016.10.046.

839

840   Violay, M., Heap, M. J., Acosta, M., & Madonna, C. Porosity evolution at the brittle-ductile
841   transition in the continental crust: Implications for deep hydro-geothermal circulation. *Scientific
842   reports*. **7(1)**, 1-10 (2017). https://doi.org/10.1038/s41598-017-08108-5.

843

844   Wanner, C., Diamond, L. W., & Alt-Epping, P. (2019). Quantification of 3-D thermal anomalies
845   from surface observations of an orogenic geothermal system (Grimsel Pass, Swiss Alps). *Journal
846   of Geophysical Research: Solid Earth*. 124(11), 10839-10854.
847   https://doi.org/10.1029/2019JB018335

848

849   Watanabe, N., Egawa, M., Sakaguchi, K., Ishibashi, T., & Tsuchiya, N. (2017). Hydraulic
850   fracturing and permeability enhancement in granite from subcritical/brittle to
851   supercritical/ductile conditions. *Geophysical Research Letters*. 44(11), 5468-5475.
852   https://doi.org/10.1002/2017GL073898.

853

854 Watanabe, N., Abe, H., Okamoto, A., Nakamura, K., & Komai, T. (2021). Formation of
855 amorphous silica nanoparticles and its impact on permeability of fractured granite in superhot
856 geothermal environments. *Scientific reports*. 11(1), 1-11.
857 https://doi.org/10.1038/s41598-021-84744-2

858

859 Wilson, M. P., Foulger, G. R., Gluyas, J. G., Davies, R. J., & Julian, B. R. (2017). HiQuake: The
860 human-induced earthquake database. Seismological Research Letters, 88(6), 1560-1565. Data set
861 https://doi.org/10.1785/0220170112 (2017). https://inducedearthquakes.org

862

863 Zareidarmiyan, A., Parisio, F., Makhnenko, R. Y., Salarirad, H., & Vilarrasa, V. (2021) How
864 equivalent are equivalent porous media? *Geophysical Research Letters*, e2020GL089163.
865 https://doi.org/10.1029/2020GL089163.

866

867 Zoback et al. (2003). Determination of stress orientation and magnitude in deep
868 wells. *International Journal of Rock Mechanics and Mining Sciences*. 40(7-8), 1049-1076.
869 https://doi.org/10.1016/j.ijrmms.2003.07.001.

870

871 Zoback, M. L. (1992). Stress field constraints on intraplate seismicity in eastern North
872 America. *Journal of Geophysical Research: Solid Earth*. 97(B8), 11761-11782.
873 https://doi.org/10.1029/92JB00221.

874

875 **Appendices**

876

877 **Appendix 1**

878
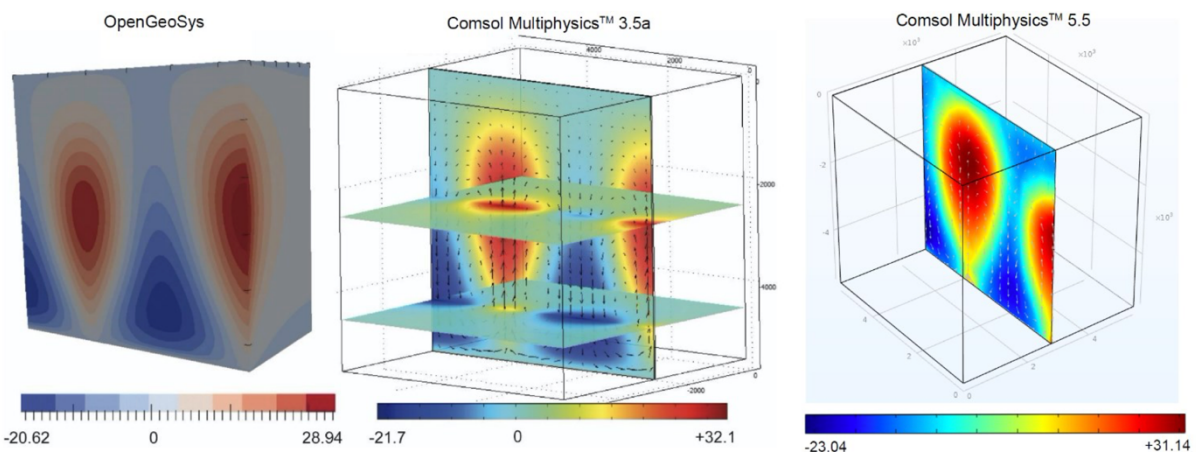
Appendix 1 : Benchmarking of our numerical experiment with the OpenGeoSys Code (Magri
et al. 2017) and Comsol Multiphysics^{TM} V3.5a (Guillou-Frottier et al. 2020) (From Duwiquet
et al. 2021).

879   The calibration of our numerical experiments was performed based on results from Comsol
880   Multiphysics^{TM} version 3.5 (Guillou-Frottier et al., 2020) as well as the OpenGeoSys numerical
881   code (Magri et al., 2017). These models consider a 40 m wide vertical fault in an impermeable
882   box (a 5.5*5.5*5.5 km side cube). The fluid properties are identical for all three results with a
883   linear dependence of temperature with water density, and an exponential decrease of viscosity
884   with temperature. This result is shown for a time $t_0 + 10^{13}$ s. The imposed permeability value is 5
885    $\times 10^{-15}$ m^2. The fluid flow velocity is 2.03×10^{-9} m.s^{-1}. The fluid flow velocity is slightly higher
886   than that described by Guillou-Frottier et al. (2020), who record a velocity of 1.4×10^{-9} m.s^{-1}.
887   The convective patterns are similar. Fluid velocity accelerates along the permeable fault and
888   exhibits upward movement due to the thermal gradient and buoyancy forces related to lower
889   water density at depth. The thermal perturbations are also within the orders of magnitude of
890   previous studies with -22.04°C and +31.14 °C.

891   The numerical experiments of Magri et al. (2017) and Guillou-Frottier et al. (2020) used Darcy's
892   law in conjunction with the equations of heat. The numerical experiments of this study couple
893   the equations of heat and mass transfer with the modulus of poroelasticity. The poroelasticity
894   interface of Comsol Multiphysics^{TM} combines Darcy's law with the linear elastic behavior of
895   porous media (details can be found in Duwiquet et al., 2021). Poroelastic coupling allows
896   boundary stresses to be imposed, which can be recorded as fluid pressure. In Appendix 1 (right),
897   no stress or other mechanical conditions are applied. Consequently, this experiment corresponds
898   to an identical coupling as in the previous studies (App 1, left and middle cases).

899

900   **Appendix 2**

901

Temperature anomaly ΔT
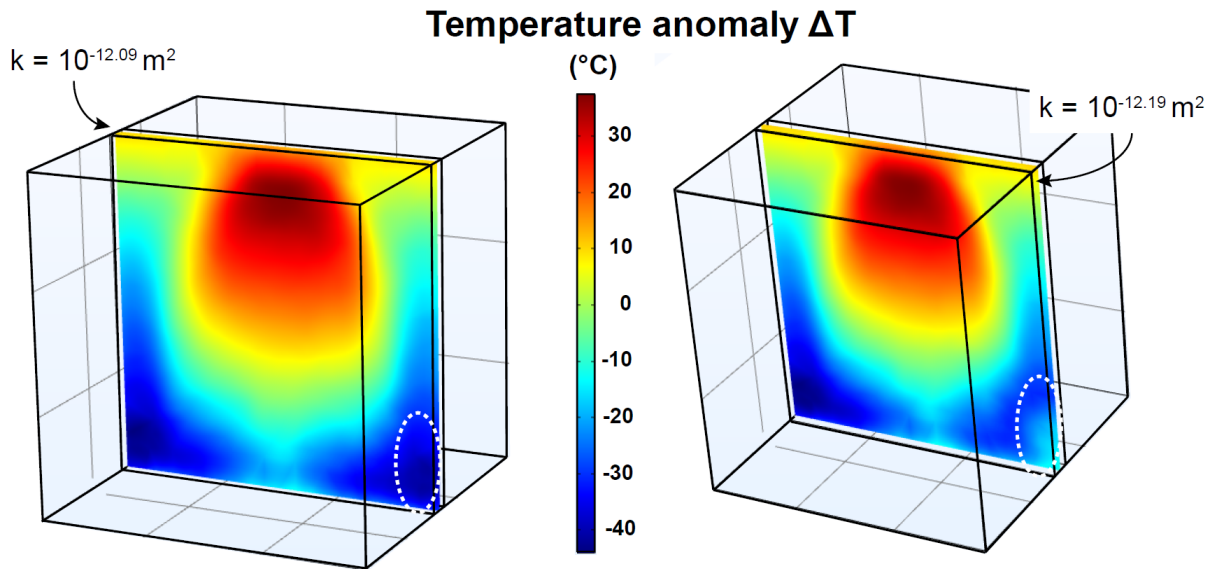
Appendix 2 : Comparison of the numerical results with a TH coupling considering as the only difference, a permeability variation of the order of $10^{-0.10}\,m^2$. The results of the numerical calculations show no difference in the calculated values (see color bar). In cross-section, parallel to the fault, the difference is only at the bottom right of the numerical model.

902   In order to understand if the permeability variations obtained after the stress application can
903   explain the differences observed between the tectonic regimes, two numerical calculations with
904   only a TH coupling have been performed. The parameters and their geometries are identical, the
905   only difference is the permeability variation. On the left, a permeability of $10^{-12.09}\,m^2$ is imposed
906   on the fault, on the right a permeability of $10^{-12.19}\,m^2$ is imposed on the fault. The results are
907   similar. The only difference is located at the bottom right of the fault. On the left, the anomaly is
908   -40°C, on the right it is -12°C. This localized difference does not seem to influence the thermal
909   distribution of the overall system.